Article

Non-Darcian Displacement of Oil by a Micellar Solution in Fractal Porous Media

Rafael Ramírez-Casco [1], René O. Vargas [2,*], Carlos Lira-Galeana [3], Edgar Ramírez-Jaramillo [3], Marcos Turcio [4] and Octavio Manero [5]

[1] School of Chemistry, National University of Mexico (FQ-UNAM), Mexico City 04510, Mexico
[2] Departamento de Termofluidos, Instituto Politécnico Nacional, SEPI-ESIME Azcapotzalco, Av. de las Granjas No. 682, Col. Santa Catarina, Alcaldía Azcapotzalco, Ciudad de México 02250, Mexico
[3] Mexican Institute of Petroleum (IMP), Mexico City 07730, Mexico
[4] National Technologic of Mexico, Queretaro 76000, Mexico
[5] Materials Research Institute, National University of Mexico (IIM-UNAM), Mexico City 04510, Mexico
* Correspondence: rvargasa@ipn.mx; Tel.: +52-55-5729-6000 (ext. 64511)

Abstract: A Buckley–Leverett analysis with capillary pressure to model the oil displacement in fractal porous media is herein presented. The effective permeability for a non-Newtonian micellar fluid is calculated by a constitutive equation used to describe the rheological properties of a displacement fluid. The main assumption of this model involves a bundle of tortuous capillaries with a size distribution and tortuosity that follow fractal laws. The BMP model predicts two asymptotic (Newtonian) regions at low and high shear and a power-law region between the two Newtonian regions corresponding to a stress plateau. Both the stress at the wall and the fluidity are calculated using an imposed pressure gradient in order to determine the mobility of the solution. We analyze different mobility ratios to describe the behavior of the so-called self-destructive surfactants. Initially, the viscosity of the displacing fluid (micellar solution) is high; however, interactions with the porous media lead to a breakage process and degradation of the surfactant, producing low viscosity. This process is simulated by varying the applied pressure gradient. The resulting equation is of the reaction–diffusion type with various time scales; a shock profile develops in the convective time scale, as in the traditional Buckley-Leverett analysis, while at longer times diffusion effects begin to affect the profile. Predictions include shock profiles and compressive waves. These results may find application when selecting surfactants for enhanced oil recovery processes in oilfields.

Keywords: Buckley–Leverett analysis; micellar solutions; fractal porous media; mobility; oil recovery

1. Introduction

Chemical-enhanced oil recovery (CEOR) is a group of techniques for improving recovery factors at the tertiary stage of the oilfield life cycle using combinations of chemical additives [1]. Surfactant flooding is a tertiary oil recovery technique that has become a useful method over the past years for obtaining additional oil production in depleted reservoirs [2,3]. The mechanism of enhanced recovery involved in polymer flooding is based on decreasing the mobility difference between the displacing and displaced fluids in order to reduce fingering effects [4]. The surfactants used in these operations display shear dependence of viscosity, thixotropy, and elasticity, among other features [5]. In contact with the porous (reservoir) structure, the flow of non-Newtonian fluids is a function of the permeability obtained by direct measurement of pressure drop and flow rate using cylindrical cores from blocks of coherent porous or granular media. The permeability obtained using a Newtonian fluid and the pressure drop/flow rate relationships are linearly related, confirming that Stokes law applies at the pore scale. When the fluid is non-Newtonian, an equivalent of Darcy's law to describe this flow musy be sought. The use of nonlinear constitutive equations aims to provide extensions of Darcy's law to cover fluids

with complex rheology [6]. At the pore scale, flow fields are strongly affected by elastic forces that cause the principal directions of the stress and strain rates to be non-parallel, as occurs with generalized Newtonian or thixotropic fluids. However, at the Darcy scale the functional over past history becomes relevant, as all complexities at the pore scale are considered in the functional.

Polymeric surfactants are macromolecules with hydrophobic and hydrophilic groups in their structural makeup; although they are polymers, their unique molecular features technically allow them to be defined as surfactants as well. Macrosurfactants, on the other hand, are of more complex molecular structure and mostly have high molecular weight. Polymeric surfactants have been proposed to reduce the number of chemical additive slugs used to implement chemical floods in oil reservoirs, as they offer operational simplicity and improve cost efficiency [4]. Polymer-free fluids based on viscoelastic surfactants have been developed to recover oil from subterranean formations. These fluids are characterized by the presence of large multi-molecular structures which provide the required high viscosity and viscoelastic properties [1]. One of the most important advantages of viscoelastic surfactants is that the multimolecular structures are broken by their interaction with produced formation fluids containing hydrocarbons. As a result, the displacing fluid can be easily removed from the propped structure. A new concept called "self-destructing" viscoelastic surfactants form large micellar structures; these have the advantage that the gel can become a low-viscosity fluid during backflow, as the individual surfactant molecules break down into oil- and water-soluble species. They can then be easily removed by back-flowing formation fluids [7,8]. These self-destructing surfactants have been the subject of research for a long time following the pioneering work of [9,10]. Depending on the rheology of these fluids, their viscosity is a function of the applied pressure gradient. Micellar solutions have a complex rheology that can be used to improve the flow of the displaced oil fluid. These surfactants exhibit pressure gradient-dependent properties, such as the presence of a shear stress plateau at a critical value of the pressure gradient. This means that at this critical stress level the flow rate increases dramatically, resulting in increased oil production. For higher pressure gradients, the shear-thinning properties of the fluid lead to viscosities even lower than those of the oil phase, up to the situation where water displaces oil [11,12].

We have previously modeled the rheology of micellar solutions, including surfactants with self-destructive properties [13]. As mentioned, the presence of a stress plateau signals the large decrease in viscosity observed in these micellar fluids at a critical pressure gradient. The modeling does not take into account the chemistry associated with the surfactant breakage process; instead, the viscosity drop is predicted by increasing the applied stress or pressure gradient. The important parameter in oil displacement by a micellar solution is the mobility ratio (i.e., the mobility of the oil phase divided by the mobility of the micellar solution, which is a non-Newtonian fluid) [14,15]. At low pressure gradients, the mobility of the surfactant solution is small, giving rise to a large mobility ratio; as a Newtonian fluid, the viscosity of the oil phase is constant. As the pressure gradient increases, the mobility of the surfactant solution increases, leading to a decrease in the mobility ratio. The limit of this decrease (a very small ratio) corresponds to the situation where the viscoelastic properties of the surfactant are destroyed and the resulting low viscosity system can be easily removed through a backflow operation [7].

The conventional methods based on Euclidean geometry and fractal geometry have shown evident advantages for addressing the complexity and multiple scales of porous media [16]. Fractal geometry has been successfully applied to characterize the structures of transport processes in porous media [17]. As far as permeability is concerned, a series of models for porous media aim to reproduce the relevant features of real porous media. The fractal geometry theory characterizes irregular or disordered objects such as sandstone pores and grains, and represents a useful tool for analysis of porous media [18,19]. Models usually relate structural parameters of porous media, such as fractal dimensions, tortuosity fractal dimensions, microstructural parameters, and porosity, to the rheological material

functions. These models seek relationships among the average flow velocity, effective permeability, effective porosity, pressure gradient, and material constants [20].

In this work, a Buckley–Leverett analysis with capillary pressure to model the oil displacement in a porous medium is presented. The model involves a bundle of tortuous capillaries with a size distribution and tortuosity that follow fractal scaling laws. The displacement of oil by a micellar solution in a fractal porous medium is described by the Bautista–Manero–Puig (BMP) model [6,21]. This model of capillary pressure allows the different shock profiles that may be present in a real porous medium to be described. Here, we use the definition of the mobility ratio M as the mobility of the oil phase/mobility of the micellar solution. Elsewhere, the definition of mobility ratio is $1/M$. In the discusion section, we provide an alternate interpretation using $1/M$ as the mobility ratio.

2. Rheological Equation of State

The BMP model is described by the following equations [21]:

$$\underline{\underline{\sigma}} + \frac{1}{G_0 \varphi} \overset{\triangledown}{\underline{\underline{\sigma}}} = \frac{2}{\varphi} \underline{\underline{D}}, \tag{1}$$

$$\frac{d\varphi}{dt} = \frac{1}{\lambda}(\varphi_0 - \varphi) + k_0(\varphi_\infty - \varphi)\underline{\underline{\sigma}} : \underline{\underline{D}}, \tag{2}$$

where $\overset{\triangledown}{\underline{\underline{\sigma}}}$ is the upper-convected derivative of the stress tensor, $\underline{\underline{D}}$ is the symmetric part of the rate of the strain tensor, φ is the fluidity (inverse of the shear viscosity η), $\varphi_0\left(\eta_0^{-1}\right)$ is the zero-shear-rate fluidity, φ_∞ is the fluidity at high shear rates, G_0 is the shear modulus, λ is the structural characteristic time, and k_0 is a kinetic constant related to structure modification. The upper-convected derivative of the stress tensor is

$$\overset{\triangledown}{\underline{\underline{\sigma}}} = \frac{d\underline{\underline{\sigma}}}{dt} - \left(\underline{\underline{L}} \cdot \underline{\underline{\sigma}} + \underline{\underline{\sigma}} \cdot \underline{\underline{L}}^T\right), \tag{3}$$

where $\underline{\underline{L}}$ is the velocity gradient tensor. Equations (1) and (2) reduce to the upper-convected Maxwell model when $\varphi \equiv \varphi_0$. These equations express that the nonlinear viscoelastic processes contained in the Maxwell equation are coupled with an equation written in terms of the fluidity, which is itself a kinetic equation with a characteristic time related to structure formation λ and a destruction term related to structure modification with a kinetic constant k_0 proportional to the dissipation. Under simple shear flow, the above equations reduce to

$$\sigma + \frac{1}{G_0 \varphi} \frac{d\sigma}{dt} = \frac{\dot{\gamma}}{\varphi}, \tag{4}$$

$$\frac{d\varphi}{dt} = \frac{1}{\lambda}(\varphi_0 - \varphi) + k_0(\varphi_\infty - \varphi)\sigma\dot{\gamma}, \tag{5}$$

where $\dot{\gamma}$ is the shear rate and the nonlinear terms in Equation (3) are not considered, which implies that the normal stresses generated under flow are negligible. In steady state, both Equations (4) and (5) can be reduced to provide

$$(\varphi_0 - \varphi) + k_0\lambda(\varphi_\infty - \varphi)\sigma\dot{\gamma} = 0. \tag{6}$$

Equation (6) predicts shear-thinning behavior when $\varphi_\infty > \varphi_0$, shear-thickening behavior when $\varphi_\infty < \varphi_0$, and Newtonian behavior when $\varphi_\infty = \varphi_0$. A plateau region is predicted in the limits of very low and very high shear rates, with a power-law behavior at the intermediate shear rates. In addition, a stress plateau is predicted when $\varphi_0 = 0$. This implies a constant stress in the limit as the shear rate approaches zero. An apparent yield is

predicted for very small values of φ_0. The physical meaning of Equation (6) can be revealed if it is written in terms of the non-dimensional dissipation, as follows:

$$k_0 \lambda \sigma \dot{\gamma} = \frac{\varphi - \varphi_0}{\varphi_\infty - \varphi} \quad \varphi < \varphi_\infty. \tag{7}$$

Upon increasing dissipation $\varphi \to \varphi_\infty$, while for decreasing dissipation $\varphi \to \varphi_0$. From Equation (6), the plateau stress can be calculated when $\varphi_0 = 0$ in the region of very small shear rates. This results in

$$\sigma_y = (k_0 \lambda \varphi_\infty)^{-1/2}, \tag{8}$$

Equation (6) can be solved for φ by expressing the results in terms of the plateau stress to provide

$$\frac{\varphi(\sigma)}{\varphi_0} = \frac{\varphi_\infty / \varphi_0}{2\sigma^2 / \sigma_y^2} \left\{ \left(\sigma^2/\sigma_y^2 - 1 \right) \pm \left[\left(\sigma^2/\sigma_y^2 - 1 \right)^2 + 4\varphi_0/\varphi_\infty \left(\sigma^2/\sigma_y^2 \right) \right]^{1/2} \right\}. \tag{9}$$

The three independent parameters in Equation (9) can be evaluated from the flow curve itself in the form of the viscosity versus the shear rate. The fluidity at low strain rates φ_0 (inverse viscosity) is extracted from the first Newtonian plateau at vanishing shear rates, and the fluidity at an infinite shear rate φ_∞ corresponds to the plateau at high shear rates. When the plateau stress is approached, the viscosity tends to a slope of -1 in a log–log plot. The usual form from which the plateau stress is evaluated considers the plateau that is exhibited as the shear rate tends to zero in a plot of the log stress versus log shear rate. In this context, the model does not contain fitting parameters. We can calculate the fluidity at the plateau stress by setting $\sigma^2/\sigma_y^2 = 1$; this provides

$$\varphi(\sigma_y) = \sqrt{\varphi_0 \varphi_\infty}. \tag{10}$$

According to the model presented here, the pores are considered as capillaries with different diameters. The change in capillary radius is taken into account by modifying the tortuosity along the flow trajectories, and several results are shown in which changes in tortuosity or fractal dimensions are considered. Although transient flow exists in a real porous medium (i.e., complex expansion–contraction trajectories), in this model the change in geometry which modifies trajectories is considered as a change in tortuosity and a change in fractal dimensions. In other words, following the averaging procedures considered in the present model, the overall flow may be considered steady; however, locally it is intrinsically unsteady. This transient state is taken into account by the variation in thew tortuosity or fractal dimensions of the porous medium in time scales shorter than that of the global averaged macroscopic flow.

2.1. Calculation of Mobility

The procedure to calculate the mobility in a complex fluid is outlined in (the appendix of reference [6]). A momentum balance on a differential element in cylindrical geometry leads to a relationship between the shear stress and the pressure gradient; in this case, the shear stress at wall in tortuous capillaries is provided by [22,23].

$$\sigma_w = -\frac{r}{2} \frac{dp}{dL_t}. \tag{11}$$

Following the fractal scaling method, the wall shear stress is [6]

$$\sigma_w = \frac{-r^{D_T}}{2^{2-D_T}} \frac{1}{D_T L_0^{D_T-1}} \frac{dp}{dL_0}, \tag{12}$$

where D_T is the fractal dimension describing the tortuous length of the capillary. Darcy's law may then be written in terms of the non-Newtonian mobility as follows:

$$v = -M_{NN} \frac{dp}{dL_0},$$
(13)

where

$$M_{NN} = k_e \varphi(\sigma).$$
(14)

As the capillaries in porous media are tortuous, the total shear stress in Equation (12) at all capillary walls is related to the fractal dimensions D_f and D_f, microstructual parameters, and pressure gradient (see [6]). The resulting effective permeability is

$$k_e = \frac{2^{2D_T - 2} \phi \left(3 - D_T - D_f \right)}{D_T L_0^{2D_T - 2} r_{\max}^{3 - D_T - D_f} \left[1 - \left(\frac{r_{\min}}{r_{\max}} \right)^{3 - D_T - D_f} \right]} \frac{1}{\varphi(\sigma)} \int_{r_{\min}}^{r_{\max}} \varphi(r) r^{D_T - D_f - 2} dr.$$
(15)

The Newtonian permeability may be obtained as a particular case when $\varphi(r) = \varphi_N r^4 / 8$, $\varphi(\sigma) = \varphi_N$ (Poiseuille's law), yielding

$$k_e = \frac{2^{2D_T - 2} \phi \left(3 - D_T - D_f \right)}{D_T L_0^{2D_T - 2} \left[1 - \left(\frac{r_{\min}}{r_{\max}} \right)^{3 - D_T - D_f} \right]} \left(\frac{r_{\max}^{2D_T}}{D_T - D_f + 3} \right).$$
(16)

In straight capillaries, $D_T = 1$; therefore, we can obtain

$$k_e = \frac{\phi \left(2 - D_f \right)}{8 \left[1 - \left(\frac{r_{\min}}{r_{\max}} \right)^{2 - D_f} \right]} \left(\frac{r_{\max}^2}{4 - D_f} \right).$$
(17)

This equation agrees with those of the current literature for Newtonian fluids. We obtained an analytical result for the permeability provided $\varphi(r)$ can be calculated [6]. This may be achieved assuming that the fluidity in the pore/capillary attains a minimum in the center of the geometry and reaches a maximum at the walls, i.e.,

$$\varphi(\xi) = \varphi_0 + (\varphi(\sigma) - \varphi_0)\xi^2.$$
(18)

Accordingly, the fluidity attains its minimum at the capillary center (at $\xi = 0$), that is, φ_0, and its maximum at the walls (at $\xi = 1$), $\varphi(\sigma)$. The fluidity at the wall requires the calculation of the wall stress according to Equation (11). Thus, the final result is [6]

$$k_e = \frac{2^{2D_T - 2} \phi \left(3 - D_T - D_f \right)}{D_T L_0^{2D_T - 2} \left[1 - \left(\frac{r_{\min}}{r_{\max}} \right)^{3 - D_T - D_f} \right]} \frac{1}{\varphi(\sigma)} \left[\frac{\varphi_0}{8} \frac{r_{\max}^{2D_T}}{D_T - D_f + 3} + \frac{\varphi(\sigma) - \varphi_0}{8} \frac{r_{\max}^{2D_T}}{D_T - D_f + 5} \right].$$
(19)

When $\varphi(\sigma) \to \varphi_0$, next to the capillary center, the permeability tends to the Newtonian constant value provided by Equation (16). Near the wall, $\varphi(\sigma)$ tends to a maximum value and the permeability diminishes asymptotically to another constant value as a function of the maximum fluidity. By defining

$$K_1 = \frac{2^{2D_T - 2} \phi \left(3 - D_T - D_f \right) r_{\max}^{2D_T}}{8 D_T L_0^{2D_T - 2} \left[1 - \left(\frac{r_{\min}}{r_{\max}} \right)^{3 - D_T - D_f} \right]}; \quad K_2 = \frac{1}{\left(D_T - D_f + 3 \right)}; \quad K_3 = \frac{1}{\left(D_T - D_f + 5 \right)},$$
(20)

Equation (19) can be expressed as

$$k_e = \frac{\varphi_0}{\varphi(\sigma)}(K_1 K_2 - K_1 K_3) + K_1 K_3. \tag{21}$$

Clearly, within the limit $\varphi(\sigma) \to \varphi_0$ the permeability is constant, providing

$$K_N = K_1 K_2. \tag{22}$$

In straight capillaries $(D_T = 1)$,

$$K_1 = \frac{\varphi\left(2 - D_f\right)r_{\max}^2}{8\left[1 - \left(\frac{r_{\min}}{r_{\max}}\right)^{2-D_f}\right]} \quad \text{and} \quad K_2 = \frac{1}{\left(4 - D_f\right)}, \tag{23}$$

which agrees with Equation (17). The non-Newtonian fluid mobility in Equation (14) becomes

$$M_{NN} = \varphi_0(K_1 K_2 - K_1 K_3) + \varphi(\sigma)K_1 K_3, \tag{24}$$

which reduces to the Newtonian mobility

$$M_N = \varphi_N(K_1 K_2), \tag{25}$$

where φ_N is the fluidity of the Newtonian fluid, while the mobility ratio becomes

$$M = \frac{M_N}{M_{NN}} = \frac{\varphi_N}{\varphi_0}\left[1 + \frac{K_3}{K_2}\left(\frac{\varphi(\sigma)}{\varphi_0} - 1\right)\right]^{-1}. \tag{26}$$

In Equation (26), the ratio is

$$\frac{K_3}{K_2} = \frac{D_T - D_f + 3}{D_T - D_f + 5}. \tag{27}$$

The limits of Equation (26) consider expressions at low and high stresses; in the low range, $\varphi(\sigma) \to \varphi_0$ and $M(\sigma \to 0) = \varphi_N/\varphi_0$. At the upper stress limit, $\varphi(\sigma) \to \varphi_\infty$, and hence

$$M(\sigma \to \infty) = \frac{\varphi_N}{\varphi_0}\left[1 + \frac{K_3}{K_2}\left(\frac{\varphi_\infty}{\varphi_0} - 1\right)\right]^{-1} \approx \frac{K_2}{K_3}\frac{\varphi_N}{\varphi_\infty}, \tag{28}$$

At the plateau stress,

$$M(\sigma_y) \approx \frac{K_2}{K_3}\frac{\varphi_N}{\sqrt{\varphi_0 \varphi_\infty}}. \tag{29}$$

In Figure 1, a plot of the normalized fluidity as a function of the stress normalized by the yield stress is disclosed. We consider a Newtonian fluid with viscosity ten times smaller than that of the non-Newtonian fluid at small stresses. As the stress increases, the fluidity of the non-Newtonian fluid increases as well, overtaking that of the Newtonian fluid. In Figure 2, the mobility ratio is plotted with the applied stress.

We define the following relative permeabilities:

$$k_{r1} = \frac{k_1}{k_{c1}}, \tag{30}$$

$$k_{r2} = \frac{k_2}{k_{c2}}, \tag{31}$$

where k_{ri} is the relative permeability of fluid i and k_{c1} is the characteristic permeability of fluid i. Figure 3 shows the variation of the relative permeabilities as a function of the saturation.
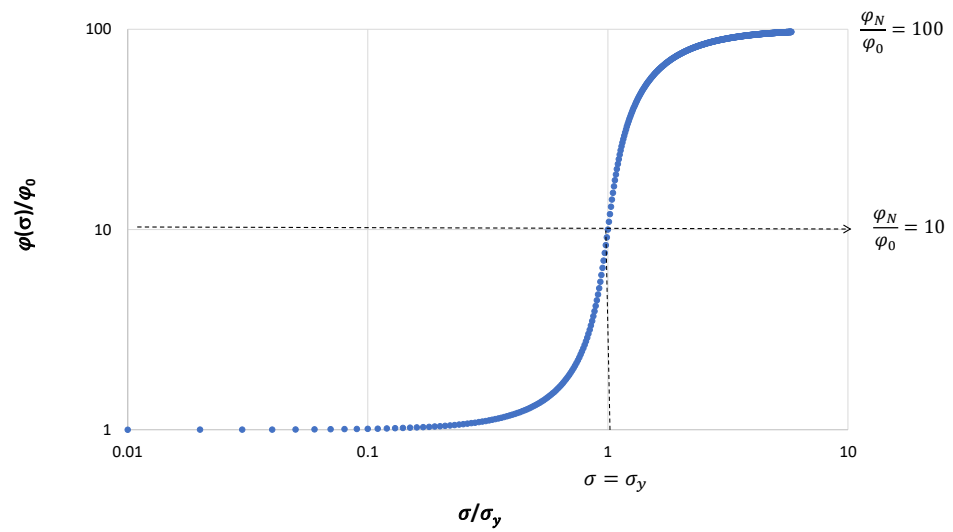
Figure 1. Normalized fluidity as a function of the stress normalized by the plateau stress. When the normalized stress is equal to one, the fluidity is $(\varphi_\infty/\varphi_0)^{1/2} = 10$, which coincides with $\varphi_N/\varphi_0 = 10$.
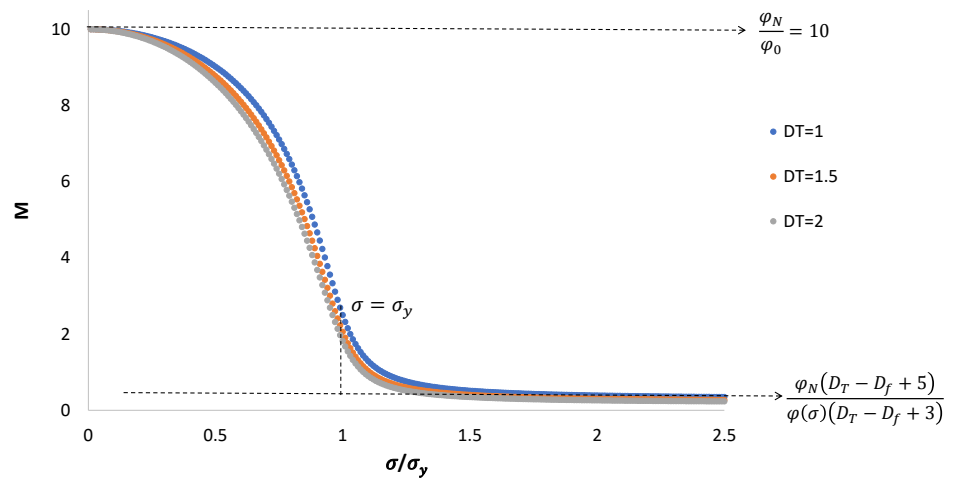
Figure 2. Mobility ratio as a function of applied stress. For small stresses, the relative mobility is $M(\sigma \to 0) = \frac{\varphi_N}{\varphi_0} = 10$. For high stresses, the relative mobility is $M(\sigma \to \infty) = \frac{K_2}{K_3} \frac{\varphi_N}{\varphi_\infty} = 0.2$. At the plateau stress, $M = \frac{K_2}{K_3} \frac{\varphi_N}{\sqrt{\varphi_0 \varphi_\infty}} = 2$. $\frac{K_2}{K_3}$ and the ratio is variable.
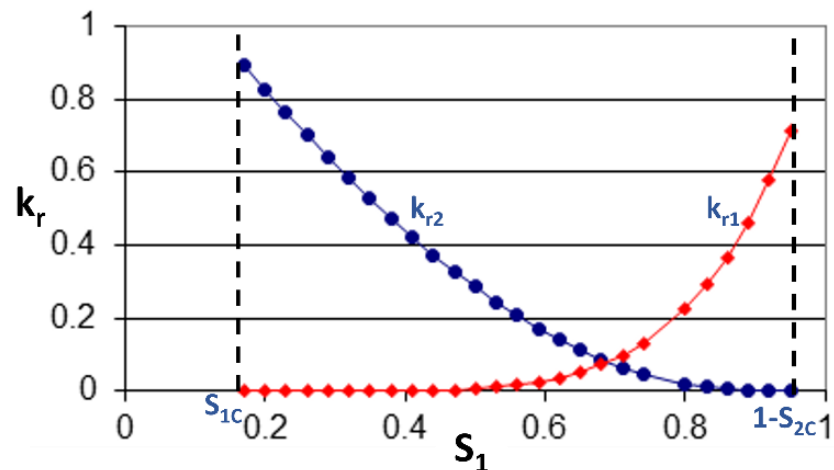
Figure 3. Relative permeabilities of Fluids 1 and 2.

Saturation limits are S_{1C} for Fluid 1 such that $1 - S_{2C}$ is the maximum saturation of Fluid 1 and the minimum saturation of Fluid 2. Figure 3 shows that there is a quadratic dependence of the relative permeability on the saturation, and therefore the following relations represent this variation:

$$k_{r1} = \alpha S_1^2, \tag{32}$$

$$k_{r2} = \alpha(1 - S_1)^2 \tag{33}$$

from the material balance for the two fluids, namely,

$$S_1 + S_2 = 1. \tag{34}$$

Upon substitution of the above equations for those of Darcy's law for each fluid provides the following displacement velocities in the porous medium:

$$u_1 = -k_{r1}k_{c1}\varphi_1\left(\frac{\partial p_1}{\partial x}\right), \tag{35}$$

$$u_2 = -k_{r2}k_{c2}\varphi_2\left(\frac{\partial p_2}{\partial x}\right). \tag{36}$$

considering that the capillary pressure depends only on saturation

$$p_2 - p_1 = p_c(S_1), \tag{37}$$

and the flow fractions are defined as follows:

$$f_1 = \frac{u_1}{u}, \tag{38}$$

$$f_2 = \frac{u_2}{u} = 1 - f_1, \tag{39}$$

where $u = u_1 + u_2$ represents the sum of the flow rate fractions, as the flow area is the same for both fluids. Deriving Equation (37) with respect to x and solving for the pressure gradients in Equations (35) and (36), upon substitution we obtain

$$f_1(S_1) = \frac{1}{\left(1 + \frac{k_{r2}k_{c2}\varphi_2}{k_{r1}k_{c1}\varphi_1}\right)} + \frac{1}{u}\frac{k_{r2}k_{c2}\varphi_2}{\left(1 + \frac{k_{r2}k_{c2}\varphi_2}{k_{r1}k_{c1}\varphi_1}\right)}\frac{\partial p_c(S_1)}{\partial x}. \tag{40}$$

Using Equations (32) and (33) and the definition of the mobility ratio $M = \frac{k_{c2}\varphi_2}{k_{c1}\varphi_1}$, we obtain

$$f_1(S_1) = \frac{1}{\left(1 + M\frac{(1-S_1)^2}{S_1^2}\right)} + \frac{k}{u}\frac{(1-S_1)^2\varphi_2}{\left(1 + M\frac{(1-S_1)^2}{S_1^2}\right)}\frac{\partial p_c(S_1)}{\partial x}, \tag{41}$$

which can be expressed as

$$f_1(S_1) = F(S_1) + H(S_1)\frac{\partial S_1}{\partial x}, \tag{42}$$

where

$$F(S_1) = \frac{1}{\left(1 + M\frac{(1-S_1)^2}{S_1^2}\right)} \tag{43}$$

$$H(S_1) = \frac{k}{u}\frac{(1-S_1)^2\varphi_2}{\left(1 + M\frac{(1-S_1)^2}{S_1^2}\right)}\frac{\partial p_c(S_1)}{\partial x}. \tag{44}$$

From the mass balance

$$\varphi \frac{\partial S_1}{\partial t} + u \frac{\partial f_1}{\partial x} = 0,$$　(45)

the following equation is obtained:

$$\frac{\partial S_1}{\partial t} + \frac{u}{\phi}\left[\frac{\partial F(S_1)}{\partial S_1}\frac{\partial S_1}{dx} + \frac{\partial}{\partial x}\left(H(S_1)\frac{\partial S_1}{\partial x}\right)\right] = 0.$$　(46)

2.1.1. The Buckley–Leverett Equation

Neglecting the capillary forces, Equation (46) reduces to

$$\frac{\partial S_1}{\partial t} + \frac{u}{\phi}\frac{\partial F(S_1)}{\partial S_1}\frac{\partial S_1}{dx} = 0.$$　(47)

A plot of the flow fraction $F(S)$ as a function of the saturation S for the three mobility ratios considering $D_T = 1$ is shown in Figure 4.
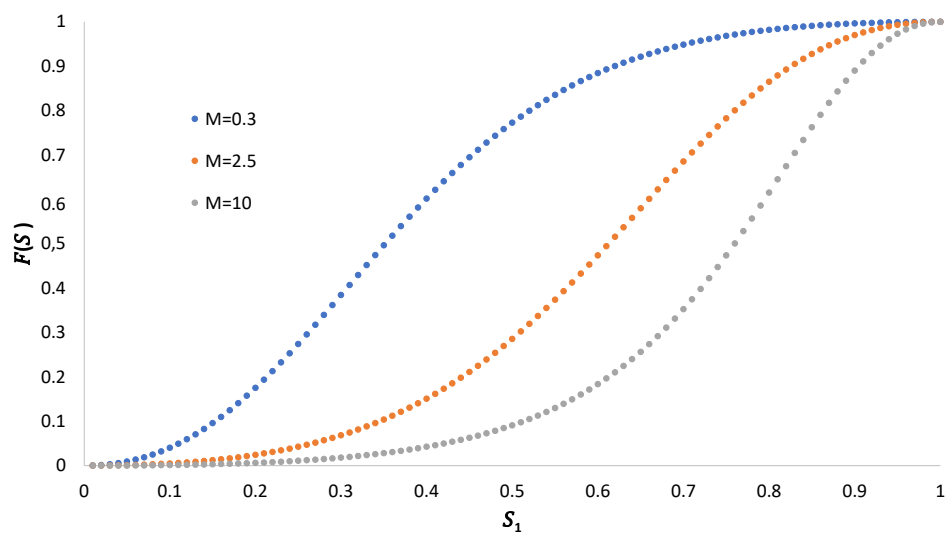
Figure 4. The flow function F as a function of saturation for three mobility ratios.

Next, we make Equation (46) non-dimensional by defining the variables $x = \frac{x'}{L}$ and $t = \frac{ut'}{\phi L}$. Dropping the sub-index, we can express Equation (46) as follows:

$$\frac{\partial S}{\partial t} + \frac{\partial F(S)}{\partial x} + \frac{\partial}{\partial x}\left(H(S)\frac{\partial S}{\partial x}\right) = 0,$$　(48)

where S refers to the saturation of Fluid 1. Up to first order in the derivatives and small capillary pressure contributions, Equation (48) leads to

$$\frac{\partial S}{\partial t} + \frac{\partial F}{\partial S}\frac{\partial S}{\partial x} = \varepsilon\frac{\partial^2 S}{\partial x^2}.$$　(49)

The Buckley–Leverett problem does not consider capillary effects:

$$\frac{\partial S}{\partial t} + \frac{\partial F}{\partial S}\frac{\partial S}{\partial x} = 0.$$　(50)

The material derivative of S in one dimension is

$$\frac{dS}{dt} = \frac{\partial S}{\partial t} + \frac{dx}{dt}\frac{\partial S}{\partial x}.$$　(51)

Comparing Equations (50) and (51), we obtain

$$\frac{dx}{dt} = \frac{\partial F}{\partial S} = r,$$

(52)

where

$$\frac{\partial F}{\partial S} = 2M \frac{S - S^2}{\left(S^2 + M(1-S)^2\right)^2}.$$

(53)

In Figure 5, we plot Equation (53) $\left(\frac{\partial F}{\partial S} \text{ versus } S\right)$ for the three mobility ratios.
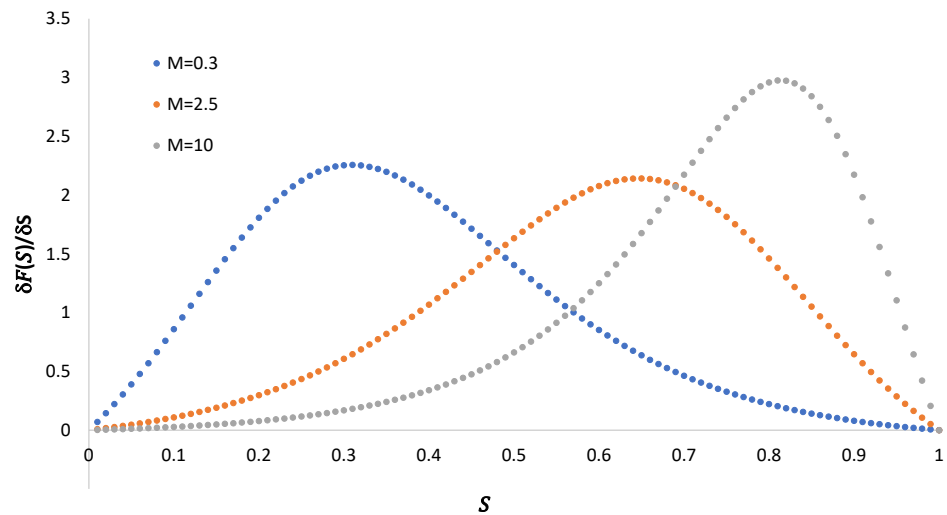
Figure 5. The derivative of $F(S)$ as a function of saturation for the three mobility ratios.

We can integrate Equation (52) as follows:

$$x = 2M \frac{S - S^2}{\left(S^2 + M(1-S)^2\right)^2} t$$

(54)

Because the function $\frac{\partial F}{\partial S}$ is not single-valued, the Buckley–Leverett analysis includes the calculation of the tangent to the flux function $F(S)$ and the presence of a shock. The tangent condition reads

$$\frac{\partial F}{\partial S} = \frac{F(S)}{S}.$$

(55)

A unique root of Equation (55) is obtained, namely,

$$\alpha = \sqrt{\frac{M}{M+1}},$$

(56)

which is the abscise of the point of intersection of the tangent and the function $F(S)$. The slope of the tangent is found from the condition

$$mS = F(S) \quad \text{or} \quad m = \frac{F(\alpha)}{\alpha},$$

(57)

and the mean saturation S_{ave} is found if $F(S) = 1$, namely,

$$S_{ave} = \frac{1}{m}.$$

(58)

In Figure 6a–c, we plot the flux function $F(S)$ and its derivative together with the tangent to locate the intersection point α.
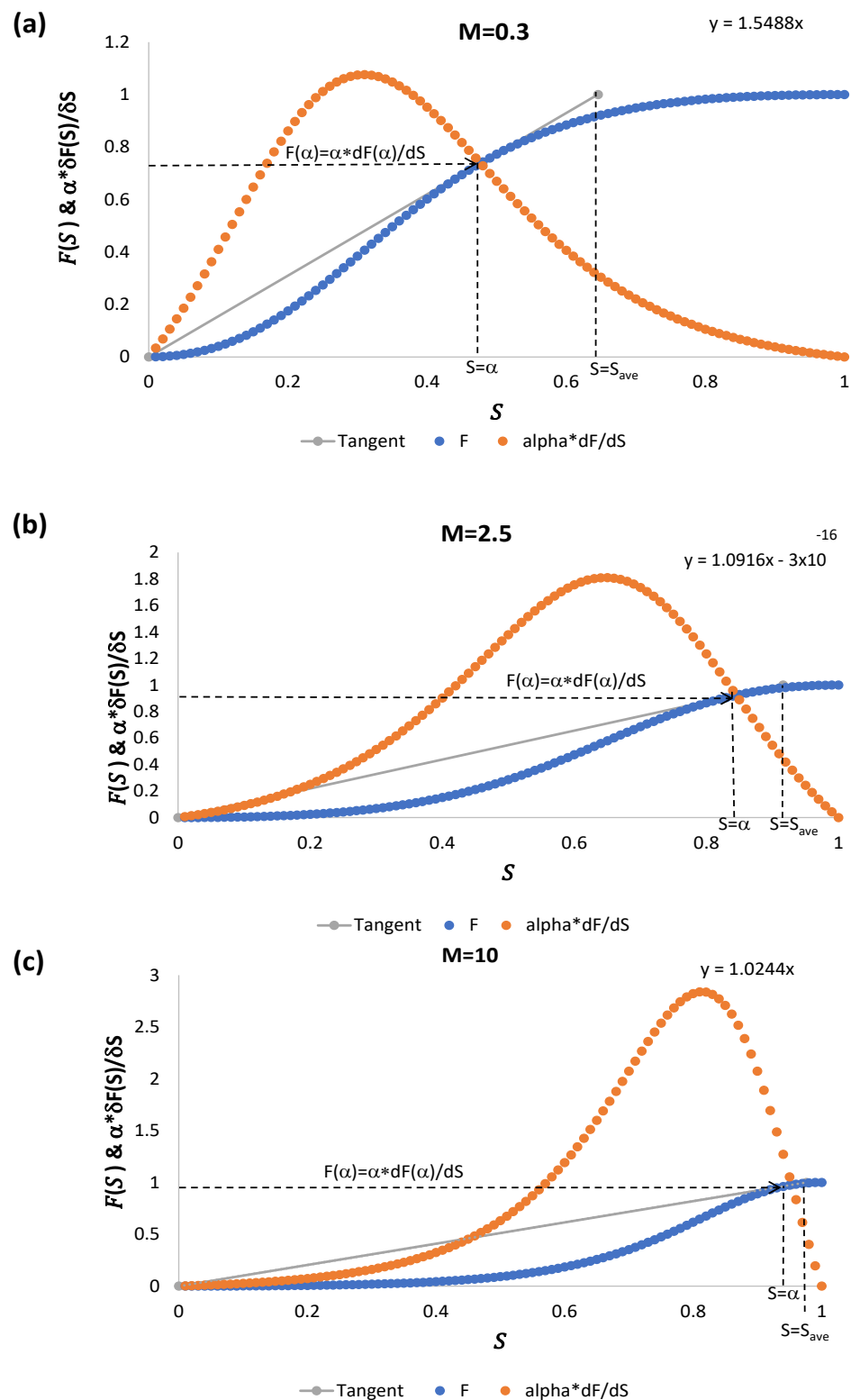
Figure 6. The function $F(S)$ and its derivative as functions of the saturation S for three mobility ratios (**a**) M=0.3, (**b**) M=2.5, and (**c**) M=10. The tangent and point of intersection with abscise α are also shown.

As the mobility ratio increases, the intersection point of the tangent and the function $F(S)$ has ordinate $F(\alpha)$ approaching one as well as $\alpha \to 1$ see Figure 7, and hence the slope tends to $450(m = 1)$; see Table 1.

Table 1. Mobility ratios with α values and the corresponding average saturations and tangents.

M	α	S_{ave}	m
0.3	0.476	0.645	1.55
2.5	0.845	0.916	1.09
10	0.953	0.976	1.02
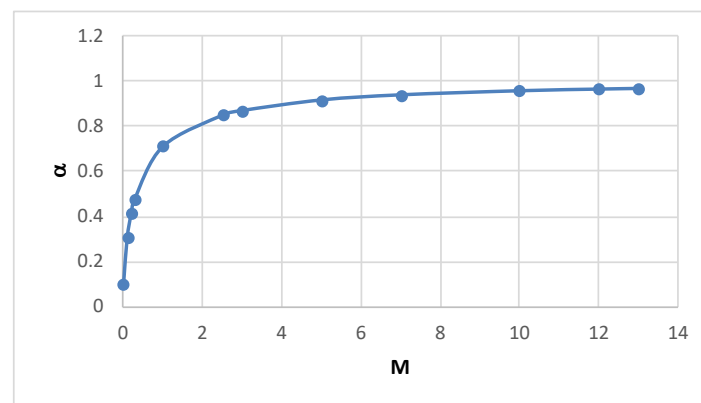
Figure 7. The root α as a function of the mobility ratio.

In Figures 1 and 2, it is clear that for low pressure gradients (namely, small stresses) the fluidity of the displacing fluid is small and the ratio of its fluidity with the fluidity of the Newtonian oil is large ($M = 10$). The plateau stress of the micellar fluid coincides with that of the oil, with a mobility ratio around 2. For high pressure gradients, the fluidity of the non-Newtonian fluid is large (close to that of water), even larger than that of the oil. In this case the displacing action of the displacing fluid decreases, which is convenient for actual enhanced oil recovery operations. It is worth mentioning that the viscosity of the displacing fluid should be properly adjusted along with the applied pressure gradient in order to provide the optimal oil displacement. This is one of the advantages of a complex non-Newtonian fluid, which provides multiple options for actual oil operations.

The equal area criterion is used to specify the value at which the shock should occur, namely,

$$\frac{\partial F(S^*)}{\partial S} = \frac{1}{S_f} \int_0^{S_f} \frac{\partial F(S)}{\partial S} dS, \tag{59}$$

where $f'(S^*)$ denotes the ordinate at which the equal area criterion holds. Equation (59) is an illustration of the mean value theorem of integrals. In fact, if $\frac{\partial F(S^*)}{\partial S} = \frac{F(\alpha)}{\alpha}$ and $S_f = \alpha$, Equation (59) is satisfied. Therefore, the shock occurs at a value of the saturation equal to α and ordinate $\frac{F(\alpha)}{\alpha}$, which is the speed of propagation according to Equation (52). In the Figure 8a–c, the saturation is plotted as a function of the propagation speed for the three mobilities.

Figures 9a–c depict the speed of propagation of the shock profile as the mobility changes. The speed is higher as the mobility ratio decreases. This effect is expected, as the viscosity of the displacing non-Newtonian fluid is larger for $M = 10$. For higher pressure gradients the displacing fluid viscosity diminishes, allowing for larger propagation speeds. In Figure 10, the saturation is plotted with the propagation speed for the three fronts, exhibiting the effect of diminishing the viscosity of the non-Newtonian pushing fluid for large pressure gradients.
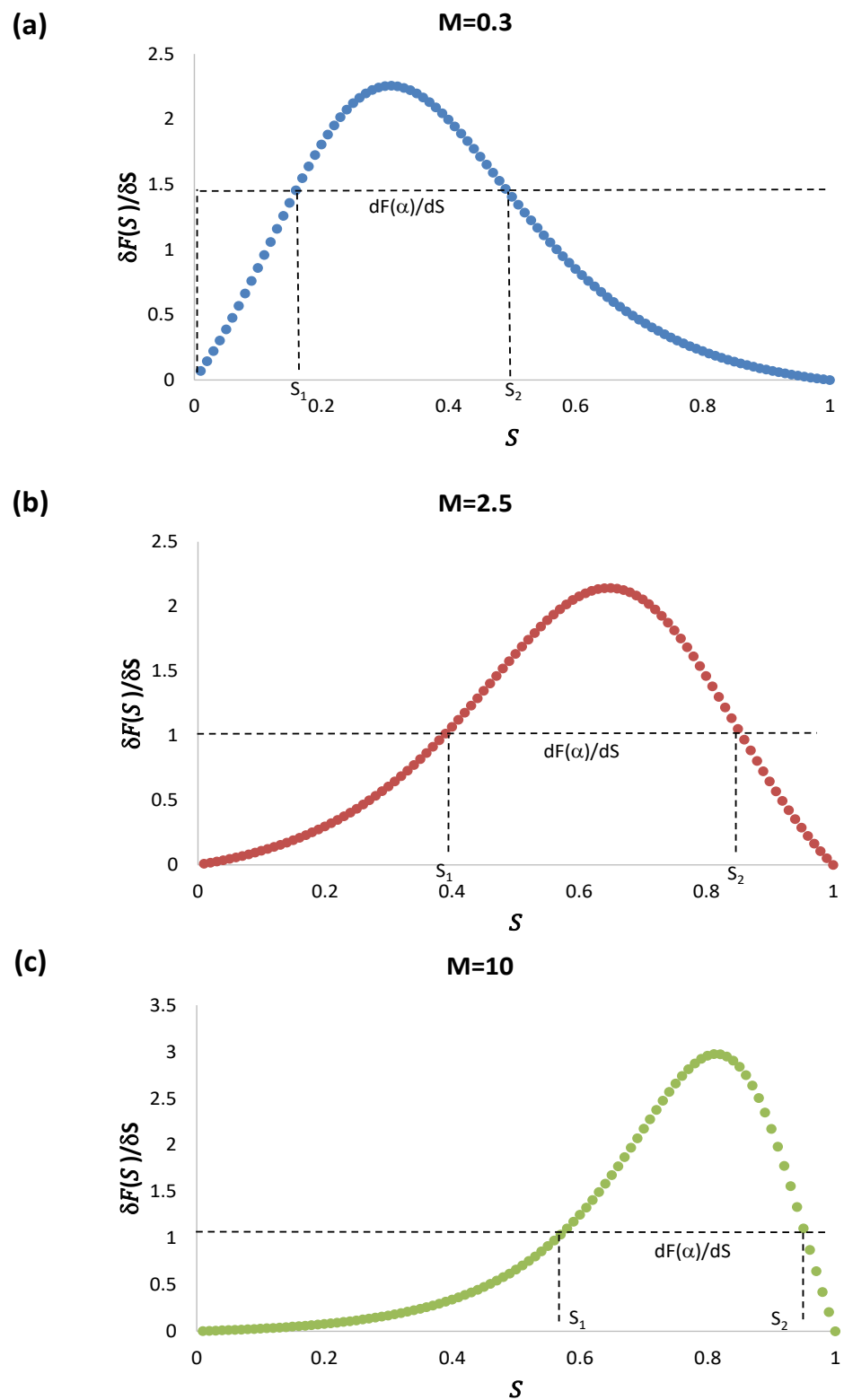
Figure 8. The derivative $\frac{\partial f}{\partial S}$ as a function of the saturation for three different mobility ratios (**a**) M = 0.3, (**b**) M = 2.5, and (**c**) M = 10, illustrating the equal areas criterion. Here, $f'(S^*)$ denotes the ordinate at which the equal area criterion holds.
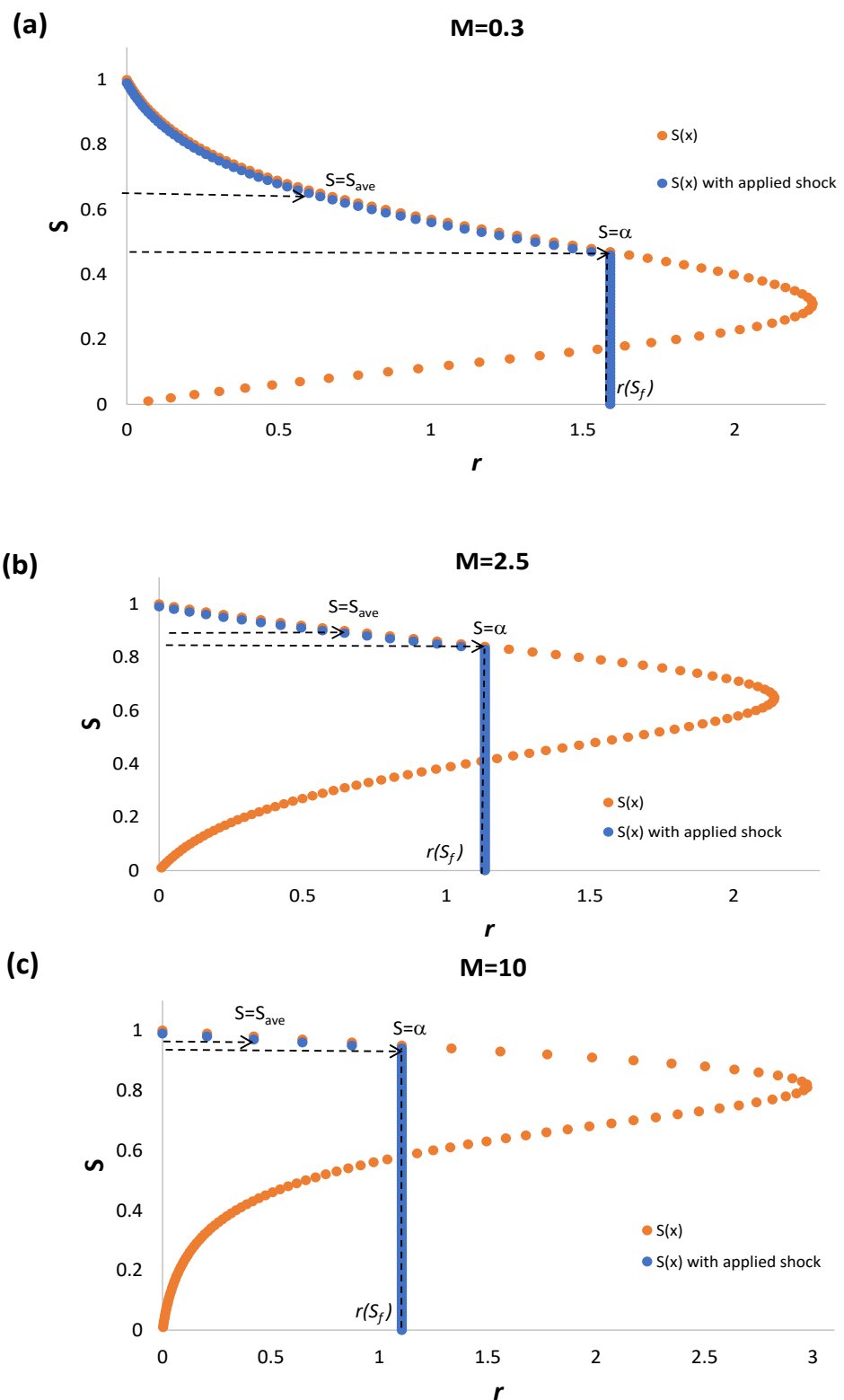
Figure 9. Saturation as a function of propagation speed for three mobility ratios (**a**) M = 0.3, (**b**) M = 2.5, and (**c**) M = 10, illustrating the location of the shock.
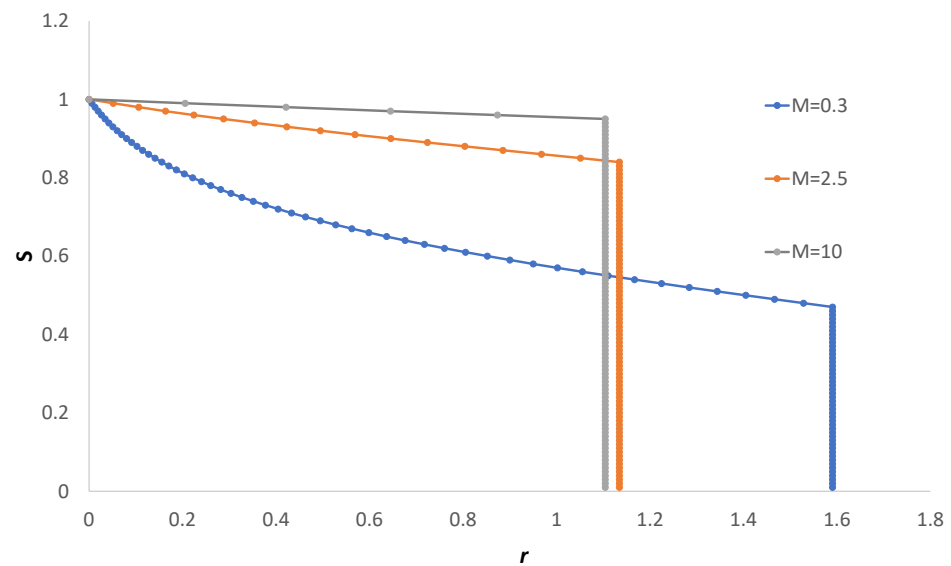
Figure 10. The velocity of the propagation front for the three mobility ratios.

To further analyse the shock profiles, let S_l be the saturation value to the left of the shock and let S_r the value of the saturation to the right of the shock; moreover, let the boundary conditions be

$$S(x,t) = S_l = S_f; x < rt, \tag{60}$$

$$S(x,t) = S_r = 0; x > rt. \tag{61}$$

The slope just before and after the shock corresponds to the Rankine–Hugoniot condition:

$$r = \frac{dx}{dt} = \frac{F(S_l) - F(S_r)}{S_l - S_r}, \tag{62}$$

if $S_f = \alpha$. Applying the boundary conditions, we obtain

$$\frac{F(S_l) - F(S_r)}{S_l - S_r} = \frac{F\left(S_f\right)}{S_f}, \tag{63}$$

which corresponds to the tangent condition. Furthermore, applying the Oleinik entropy condition

$$\frac{F(S_l) - F(S)}{S_l - S} \geq \frac{F(S_l) - F(S_r)}{S_l - S_r}, \tag{64}$$

if $S = \alpha$, $\frac{F(S_f) - F(\alpha)}{S_f - \alpha} \geq \frac{F(S_f)}{S_f}$ and $\alpha \geq S_f$. Hence, the criterion of equal areas is sufficient to define the shock location according to the Oleinik criterion.

2.1.2. Capillary Pressure

Here, we consider the model by Hassanizadeh and Gray, in which the capillary pressure can be described according to the following expression:

$$P_c(S) = p_c(S) - \tau \frac{\partial S}{\partial t}, \tag{65}$$

where $p_c(S)$ is the static capillary pressure and τ is a characteristic time. In this case, and considering that the capillary pressure in equilibrium is generally a decreasing function of saturation $p_c(S) = -S$, Equation (46) becomes:

$$\frac{\partial S}{\partial t} + \frac{\partial f(S)}{\partial x} = \frac{\partial}{\partial x}\left[H(S)\left(\frac{\partial S}{\partial x} + \tau\frac{\partial^2 S}{\partial x \partial t}\right)\right]. \tag{66}$$

We discuss an extension to the B-L equation which includes the third-order mixed derivatives term and models the capillary pressure. Travelling wave solutions exist in the extended model. The speed of the shock, S_l, and S_r are related through the Rankine–Hugoniot (RH) condition Equation (62). Experiments in two-phase flow in porous media reveal complex infiltration profiles with overshoots (i.e., non-monotone profiles). Solutions with the second derivative term exist if $f(S)$, S_r, and S_l satisfy the RH and Oleinik entropy conditions. In the limit $\varepsilon \to 0$, traveling waves converge to the shock (S_r, S_l).

If $S > \alpha$, then a weak solution is composed of a rarefaction wave in the region where $S > \alpha$ and a shock that spans the range $0 < S < \alpha$. Focusing on the relation of S_l and τ, we establish the existence of the function

$$\tau = \tau(S_l) \quad \text{defined in the interval} \quad \alpha < S_l < \beta, \tag{67}$$

where β is defined through the equal area criterion

$$\int_0^\beta \left[F(S) - \frac{F(\beta)}{\beta}S\right]dS = 0 \tag{68}$$

in such a way that Equation (66) may possess a shock wave solution in which

$$\tau(S_l) \to \tau_* > 0; S_l \to \alpha, \tag{69}$$
$$\tau(S_l) \to \infty > 0; S_l \to \beta, \tag{70}$$

in which case τ is a bifurcation parameter when $0 < \tau \le \tau_*$. For the case in which $\tau > \tau_*$, the criterion $\alpha \ge S_f$ is not fulfilled, and new types of shock waves are admissible.

With β as defined above, we establish the existence of a function $\tau(S_l)$ defined for $\alpha < S_l < \beta$ such that Equation (66) has a travelling wave solution with $S_r = 0$ if and only if $\tau = \tau(S_l)$.

The solution of Equation (66) for various cases is illustrated in the following plots; here, $x = vt(t = 1)$.

A Fortran numerical code was developed using the finite difference scheme proposed by [14]. This code was used to solve the model governing equation (see Equation (5.1) in [14]). With same parameters used by them, the computations were performed on the interval $-2 \le x \le 4$, with $\Delta x = h = 0.002$ for the rarefaction and rarefaction-under-compressive shock solutions and $h = 0.005$ in other cases. All solutions are shown at time $t = 1$ and with $\Delta t = k = 0.1(\Delta x)^2$. The numerical code was validated by comparing the cases reported by [14]. The results showed that the present code qualitatively reproduces the same results as shown in their figures.

3. Results

In Figure 11a–d we plot the first example, consisting of the case in which $S_l = 0.2$, $S_r = 0.4$, $\tau = 1$ and $\varepsilon = 0.01$, for the three mobility ratios ($M = 0.3, M = 2.5$ and $M = 10$). In Figure 11a rarefaction wave solutions are shown for high mobility ratios, becoming more shock-like as the ratio diminishes. The corresponding flux functions are illustrated in Figure 11b–d. It is clear that the front velocity increases as the mobility ratio decreases, as the slope of the curve between $S = 0.2$ to $S = 0.4$ increases from $M = 10$ to $M = 0.3$. The fact that a near shock-like solution is apparent in Figure 11b indicates that the flux curve in this region is almost a straight line.
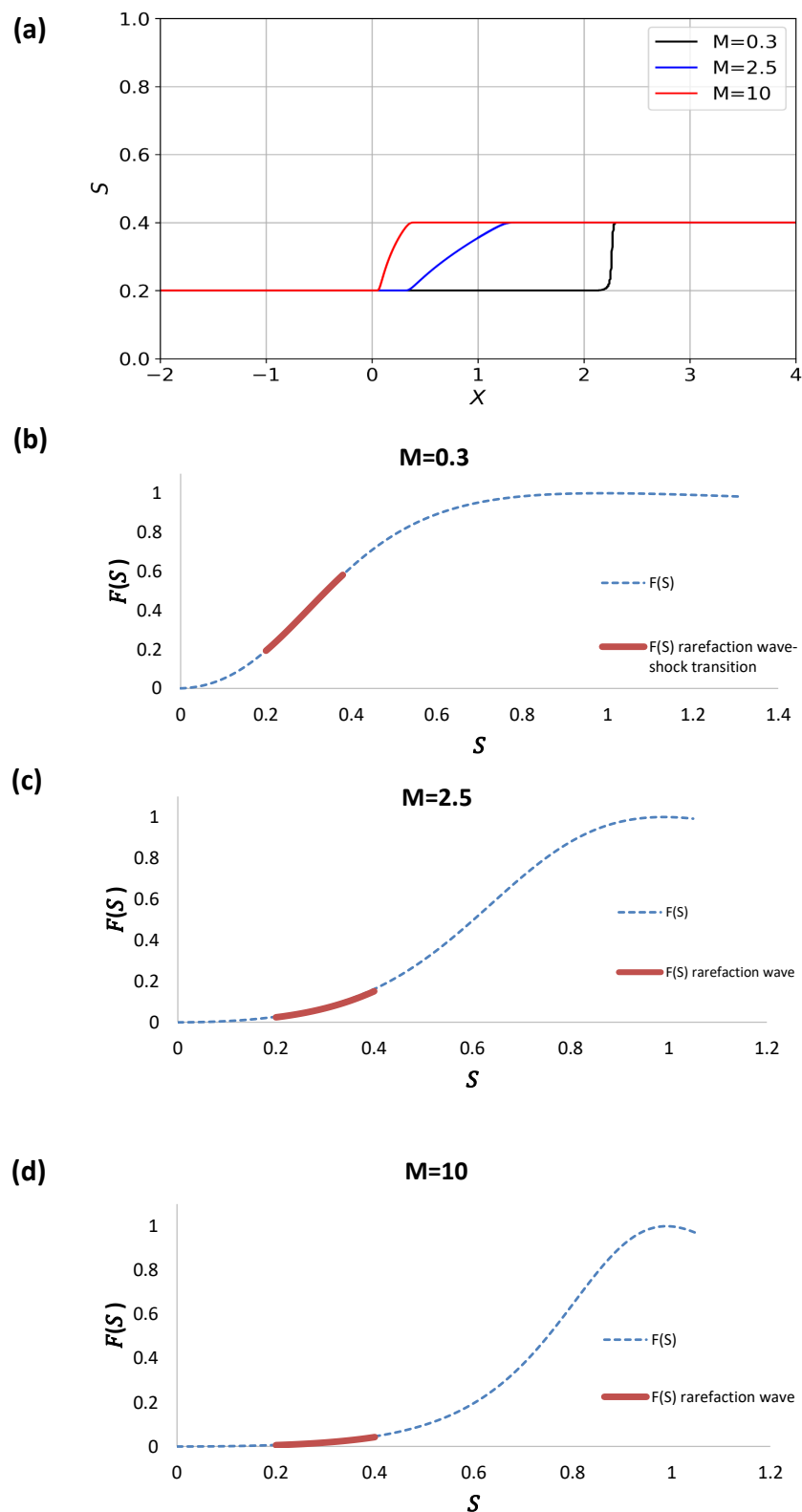
Figure 11. (**a**) Rarefaction wave solution for $S_l = 0.2$, $S_r = 0.4$, $\tau = 1$, and $\varepsilon = 0.01$. The corresponding flux functions for three different mobility ratios (**b**) M = 0.3, (**c**) M = 2.5, and (**d**) M = 10.

Figure 12a–d presents the solution for the three representative mobilities, from $S_l = 0.6$ to $S_r = 0.4$. In Figure 12a, a rarefaction wave solution is apparent at a small mobility ratio. As the mobility ratio increases, the solutions now depict shocks appearing at a relatively high propagation velocity ($M = 2$) as well as at a lower velocity ($M = 10$).
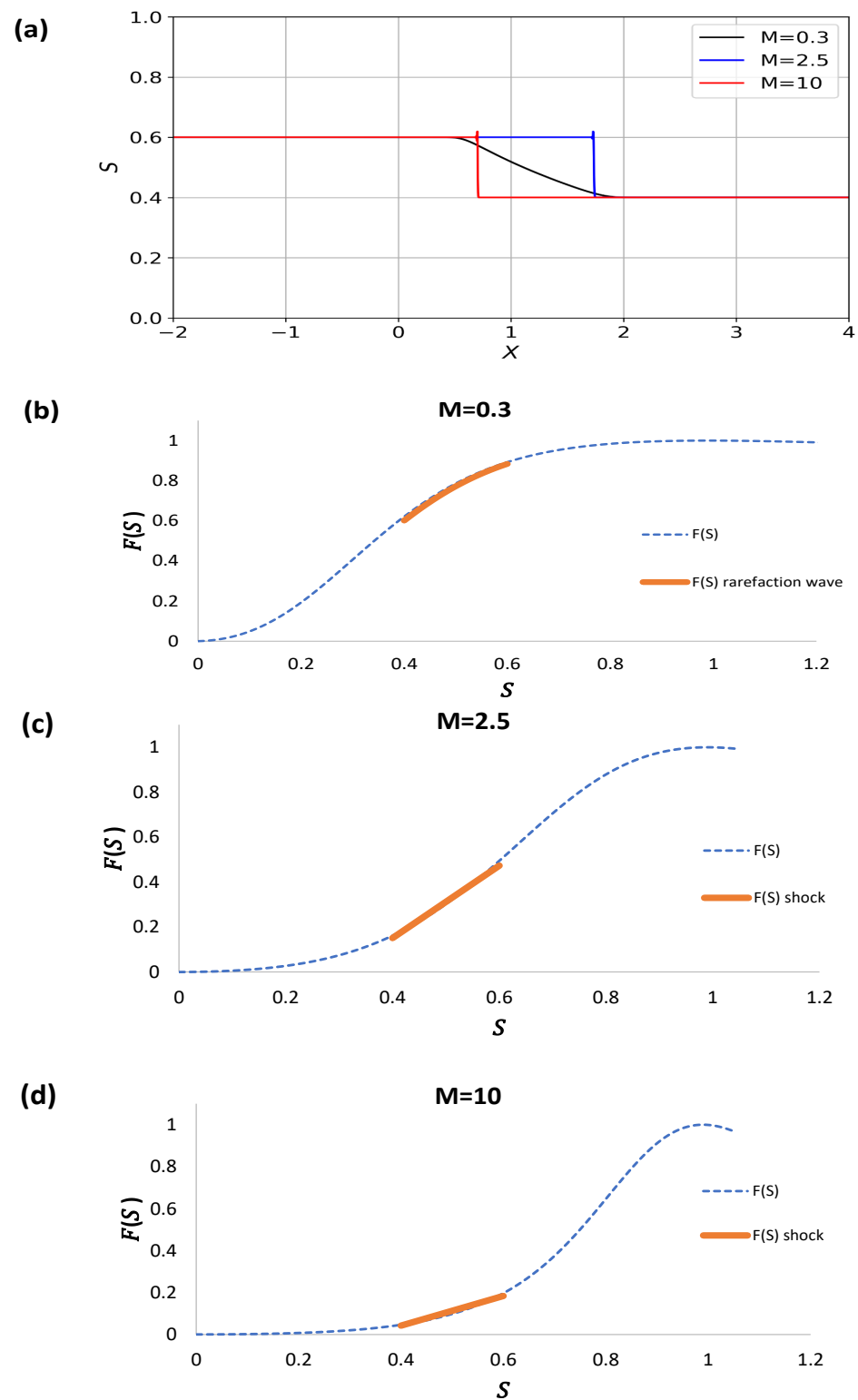
Figure 12. (**a**) Rarefaction wave which evolves into to shocks as the mobility ratio diminishes for $S_l = 0.6$, $S_r = 0.4$, and $\varepsilon = 0.05$. (**b**) The rarefaction wave location in the upper region of the flux curve. (**c**,**d**) The shocks are represented by straight lines within the saturation interval $(0.6, 0.4)$.

A more complex situation is exhibited here, as a shock trailing the under-compressive shock for $S_l = 0.8$, $S_r = 0.2$, $\tau = 1$ and $\varepsilon = 0.05$ is shown in Figure 13a–d.
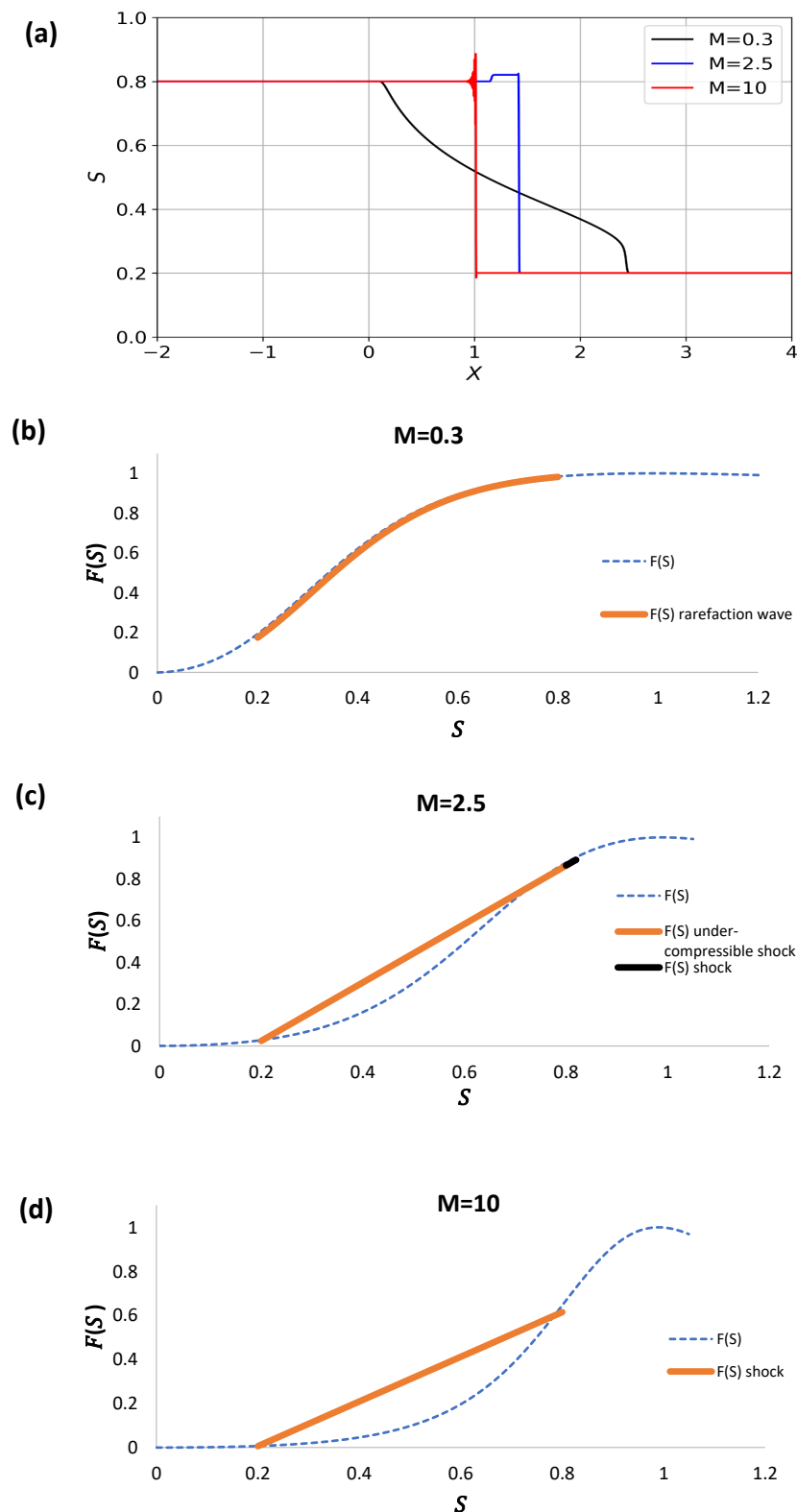
Figure 13. (**a**) The rarefaction wave evolves into a shock trailing the under-compressible shock for $M = 2.5$ and alternatively evolving into an under-compressive shock for $M = 10$. (**b–d**) The shock behaviour changes from a rarefaction wave at low mobility ratios into a small shock trailing an under-compressive shock at high mobility ratios.

For low mobility ratios, the rarefaction wave is represented in the flux curve in Figure 13b in the saturation interval $(0.8, 0.2)$. At intermediate mobility ratios $(M = 2.5)$

there is a small shock from 0.8 to 0.82 trailing the large under-compressive shock from $S = 0.82$ down to $S = 0.2$ (Figure 13c). The propagation velocity of the first shock is smaller than that of the large shock, as represented in the flux curve by a small change in the slope of the black line with respect to the higher slope of the brown straight line. For large mobility ratios, oscillations followed by an under-compressible shock from 0.8 down to 0.2 are presented.

The last example exhibits two shock profiles at low and high mobility ratios, with an under-compressive wave trailing a shock in the intermediate mobilities. Figure 14a–d illustrates the saturation as a function of the propagation velocity (Figure 14a) and the corresponding flux curves for the three mobilities (Figure 14b–d). It is interesting that the smallest mobility ratio generates a shock at lower velocity than that of the high mobility ratio. The flux curve (Figure 14b) for $M = 0.3$ describes a shock in the saturation interval $(0.9, 0.4)$, which is represented by a straight line with a slope corresponding to the abscise of the blue curve in Figure 14a. On the other hand, the flux curve for $M = 10$ (Figure 14d) describes a shock in the same saturation interval, in this case represented by the straight line, except with larger slope. The oscillations above 0.9 are due to the complex eigenvalues at S_l, as referenced in [14]. The curves corresponding to the intermediate mobility ratio $(M = 2)$ comprise a rarefaction wave from 0.9 to 0.7 trailing a shock profile from 0.7 to 0.4. This behaviour may be described by a curve that follows the flux curve from 0.9 to 0.7, trailing a straight line with the largest slope between 0.7 down to 0.4, as illustrated in Figure 14c.
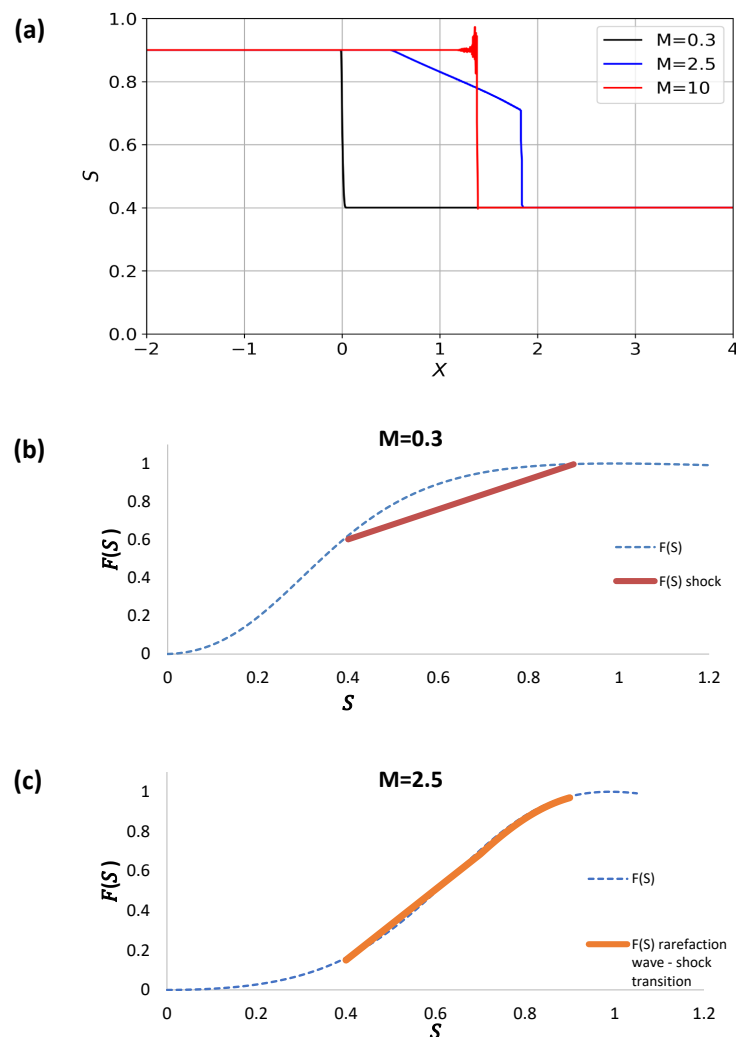
Figure 14. *Cont.*
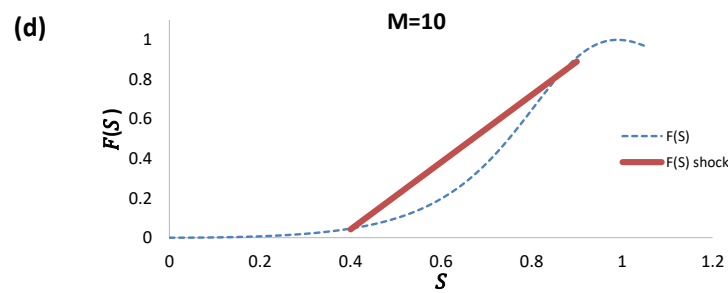
Figure 14. (**a**) The undercompressive shock for $S_l = 0.8$, $S_r = 0.2$, and $\varepsilon = 0.05$. The corresponding flux functions for three different mobility ratios (**b**) M = 0.3, (**c**) M = 2.5, and (**d**) M = 10.

The influence of the characteristic time τ in Equation (66) on the shock pattern is small, as can be observed in Figure 15. The results presented here agree with the analytical solutions in [24]. Indeed, the shifting of the flux curve as the mobility ratio changes is reproduced. The shock propagation predictions agree with present results of our analysis as well.
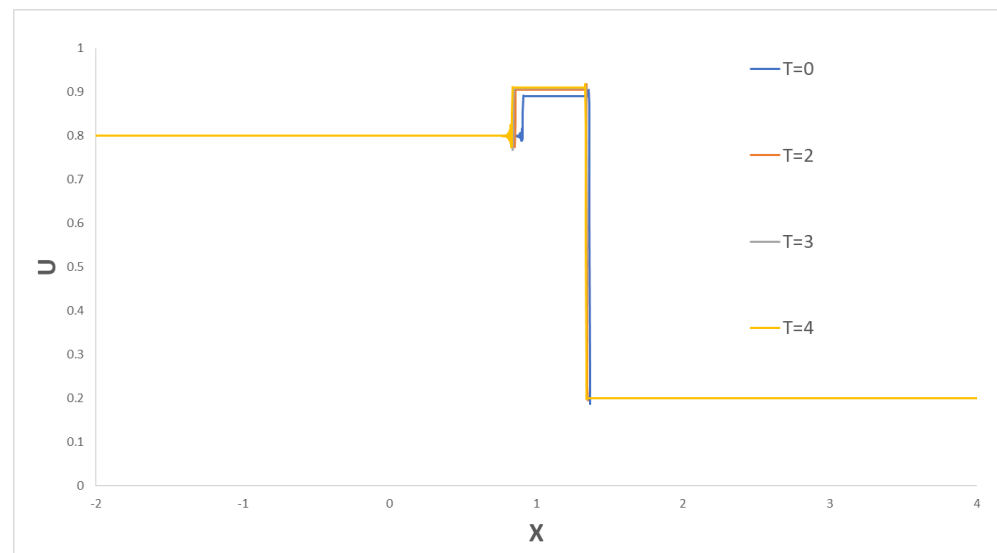
Figure 15. Saturation as a function of velocity for various values of the characteristic times τ (the same example as that described in Figure 13a for $M = 2.5$).

4. Discussion

Non-Newtonian fluids such as the micellar solution analysed here have variable viscosity that depends on the stress or pressure gradient. At low pressure gradients, the viscosity of these fluids is large, while upon increasing the pressure gradient the viscosity decreases. The viscosity drop can be quite large, in some cases more than two decades. In the process of oil displacement, the mobility ratio is one of the most important parameters, defined here as the mobility of the oil phase divided by the mobility of the non-Newtonian fluid. There are alternative definitions of the mobility ratio, namely, those that consider it as the mobility of the non-Newtonian fluid divided by the mobility of the oil phase. This definition, which according to the anonymous reviewer is conventional in the oil industry, is used to set a criterion that represents a favourable condition for ratios equal or lower than one, with ratios larger than one being unfavourable. The definition that we use here has been utilized previously in various references [14]. In fact, the presented results can be re-interpreted by substituting M^{-1} for M. In this context, the mobility ratio at low stresses in Figure 2 is small, corresponding to high viscosity (low fluidity) of the non-Newtonian fluid, which represents a favourable condition. An unfavourable condition is attained for mobility ratios larger than one, and this condition is found for stresses larger than

the yield stress, corresponding to decreased viscosity of the non-Newtonian fluid. This is an important result, as the pressure gradient can be adjusted to conveniently provide mobility ratios. As shown in Figure 10, the curve with $M = 0.3$ ($M^{-1} = 3.33$) is now unfavourable, whereas the curves with $M = 2.5$ and $M = 10$ are favourable. Subsequently, in Figures 11–14 we provide examples with various values of the saturations (S_l and S_r) for the examined mobility ratios. For mobility ratios larger than one, four examples (Figures 11b, 12b, 13b and 14b) represent unfavourable conditions consists of fronts with rarefaction waves (Figures 12b and 13b), rarefaction–shock transitions (Figure 11b), or retarded shocks (Figure 14b). These examples illustrate various situations for different regions along the flow curve for optimum oil displacement with low mobility ratios.

5. Conclusions

We performed a Buckley–Leverett analysis with capillary pressure to describe the flow patterns arising in the displacement of oil by a non-Newtonian micellar solution in a fractal porous medium. Although a number of upscaled and effective models can be used [24,25], our proposed approach provides a fast and simple description. The Darcian permeability for a Newtonian fluid generalizes to describe the flow of non-Newtonian fluids when the porous media has dimensions and tortuosity with a fractal structure. The micellar solution is a viscoelastic fluid in which the fluidity (inverse viscosity) varies with the applied pressure gradient. These ingredients provide expressions of the mobility ratio between the displacing fluid (the micellar solution) and the oil.

We use a constitutive equation for micellar fluids (the BMP model) to model the fluidity at a given shear stress or pressure gradient. This provides variations in the mobility ratio corresponding to the applied pressure gradient. Micellar solutions possess a complex rheology that can be used to improve the flow rates of the displaced oil fluid. In fact, these surfactants exhibit particular properties as the pressure gradient increases, such as the presence of a shear stress plateau at a critical value of the pressure gradient. This means that the flow rate increases drastically at this critical stress. These rheological properties allow the flow behavior to be mimicked in porous media of so-called self-destructive surfactants, which possess a high viscosity at the initial stage of the oil displacing process followed by degradation of their chemical structure, leading to a hydrophobic oil–affine structure and a hydrophilic molecule with affinity for water. The resulting solution has a small mobility ratio and low viscosity, and is easily removed from the formation.

The implementation of a Buckley–Leverett analysis with capillary pressure allows the different shock profiles that may be present in a real porous media to be described. Because the function $\frac{\partial f(S)}{\partial S}$ is double-valued, the solution to this problem is to theoretically modify the plot by defining a saturation discontinuity at x_f and then balancing the areas ahead of the front and below the curve. In other words, a discontinuity in S at a front location x_f is needed to make the saturation distribution single-valued and to provide a material balance for fluid displacement.

With capillary pressure included, a variety of shock profiles and under-compressive waves are predicted. This discontinuity propagates as combinations of shock and rarefaction waves, suggesting the decomposition of the solutions of the general initial-value problems into combinations of traveling waves (approximating shocks) and smooth waves (approximating rarefaction waves).

It is worth mentioning that the viscosity of the displacing fluid and applied pressure gradient should be properly adjusted in order to provide the optimal oil displacement. This is one of the advantages of a complex non-Newtonian fluid, which provide multiple options for actual EOR operations.

Author Contributions: Conceptualization, O.M. and R.R.-C.; Software, R.O.V. and R.R.-C.; Validation, R.R.-C.; Formal analysis, O.M., R.R.-C. and M.T.; Investigation, R.O.V., R.R.-C., C.L.-G., E.R.-J., M.T. and O.M.; Writing – review and editing, C.L.-G., E.R.-J. and O.M.; Project administration, C.L.-G.; Funding acquisition, R.O.V. All authors have read and agreed to the published version of the manuscript.

Conflicts of Interest: The authors declare no conflict of interest.

References

1. Afolabi, F.; Mahmood, S.M.; Yekeen, N.; Akbari, S.; Sharifigaliuk, H. Polymeric surfactants for enhanced oil recovery: A review of recent progress. *J. Pet. Sci. Eng.* **2022**, *208*, 109358. [CrossRef]
2. Sheng, J. Status of Surfactant EOR Technology. *Petroleum* **2015**, *79*, 97–105. [CrossRef]
3. Manrique, E.; Thomas, C.; Ravikiram, R.; Izadi, M.; Lantz, M.; Romero, J.; Alvarado, V. EOS: Current Status and Opportunities, 2010. In Proceedings of the SPE IOR Symposium, Tulsa, OK, USA, 24–28 April 2010.
4. Raffa, P.; Broekhuis, A.A.; Picchioni, F. Polymeric surfactants for enhanced oil recovery: A review. *J. Pet. Sci. Eng.* **2016**, *145*, 723–733. [CrossRef]
5. Ghannam, M.T.; Selim, M.Y.E.; Zekri, A.Y.; Esmail, N. Thixotropic Assessment of Some Enhanced Oil Recovery used Polymers. *Int. J. Eng. Res. Technol.* **2020**, *9*, 1683–1693. [CrossRef]
6. Turcio, M.; Reyes, J.; Camacho, R.; Lira-Galeana, C.; Vargas, R.; Manero, O. Calculation of effective permeability for the BMP model in fractal porous media. *J. Pet. Sci. Eng.* **2013**, *103*, 51–60. [CrossRef]
7. Othman, A.; AlSulaimani, M.; Aljawad, M.S.; Sangaru, S.S.; Kamal, M.S.; Mahmoud, M. The Synergetic Impact of Anionic, Cationic, and Neutral Polymers on VES Rheology at High-Temperature Environment. *Polymers* **2022**, *14*, 1145. [CrossRef] [PubMed]
8. Holmberg, K. (Ed.) *Novel Surfactants: Preparation, Applications, and Biodegradability*; Dekker: New York, NY, USA, 1998.
9. Lagerman, R.; Clancy, S.; Tanner, D.; Johnston, N.; Callian, B.; Friedli, F. Synthesis and performance of ester quaternary biodegradable softeners. *J. Am. Oil Chem. Soc.* **1994**, *71*, 97–100. [CrossRef]
10. Wilk, K.A.; Bieniecki, A.; Burczyk, B.; Sokolowski, A. Synthesis and hydrolysis of chemodegradable cationic surfactants containing the 1,3-dioxolane moiety. *J. Am. Oil Chem. Soc.* **1994**, *71*, 81–85. [CrossRef]
11. Wang, G.W.; Liu, Y.C.; Yuan, X.Y.; Lei, X.G.; Guo, Q.X. Preparation, Properties, and Applications of Vesicle-Forming Cleavable Surfactants with a 1,3-Dioxane Ring. *J. Colloid Interface Sci.* **1995**, *173*, 49–54. [CrossRef]
12. West, C.A.; Sanchez, A.M.; Hanon-Aragon, K.A.; Salazar, I.C.; Menger, F.M. Preparation and characterization of a simple destructible surfactant. *Tetrahedron Lett.* **1996**, *37*, 9135–9138. [CrossRef]
13. Manero, O.; Bautista, F.; Soltero, J.; Puig, J. Dynamics of worm-like micelles: The Cox-Merz rule. *J. Non-Newton. Fluid Mech.* **2002**, *106*, 1–15. [CrossRef]
14. Spayd, K.; Shearer, M. The Buckley–Leverett Equation with Dynamic Capillary Pressure. *SIAM J. Appl. Math.* **2011**, *71*, 1088–1108. [CrossRef]
15. Olajire, A.A. Review of ASP EOR (alkaline surfactant polymer enhanced oil recovery) technology in the petroleum industry: Prospects and challenges. *Energy* **2014**, *77*, 963–982. [CrossRef]
16. Mandelbrot, B. *The Fractal Geometry of Nature*; Freeman: New York, NY, USA, 1982.
17. Xu, P.; Mujumdar, A.S.; Sasmito, A.P.; Yu, B.M. Multiscale modeling of porous media. In *Heat and Mass Transfer in Drying of Porous Media*; Taylor and Francis: Oxfordshire, UK, 2019.
18. Katz, A.J.; Thompson, A.H. Fractal Sandstone Pores: Implications for Conductivity and Pore Formation. *Phys. Rev. Lett.* **1985**, *54*, 1325–1328. [CrossRef] [PubMed]
19. Wu, J.; Yu, B. A fractal resistance model for flow through porous media. *Int. J. Heat Mass Transf.* **2007**, *50*, 3925–3932. . [CrossRef]
20. Brambila, F. *Fractal Analysis*; IntechOpen: Rijeka, Croatia, 2017. [CrossRef]
21. Bautista, F.; de Santos, J.; Puig, J.; Manero, O. Understanding thixotropic and antithixotropic behavior of viscoelastic micellar solutions and liquid crystalline dispersions. I. The model. *J. Non-Newton. Fluid Mech.* **1999**, *80*, 93–113. [CrossRef]
22. Cavatorta, N.; Tonini, R.N. Dimensionless velocity profiles and parameter maps for non-Newtonian fluids. *Int. Commun. Heat Mass Transf.* **1987**, *14*, 359–369. [CrossRef]
23. Li, Y.; Yu, B.; Chen, J.; Wang, C. Analysis of Permeability for Ellis Fluid Flow in Fractal Porous Media. *Chem. Eng. Commun.* **2008**, *195*, 1240–1256. [CrossRef]
24. McWhorter, D.; Sunada, D. Exact Integral Solutions for Two-Phase Flow. *Water Resour. Res.* **1990**, *26*, 399–413. [CrossRef]
25. Andersen, P.Ø; Nesvik, E.K.; Standnes, D.C. Analytical solutions for forced and spontaneous imbibition accounting for viscous coupling. *J. Pet. Sci. Eng.* **2020**, *186*, 106717. [CrossRef]